Ferromagnetic Alloys: Magnetoresistance, Microstructure, Magnetism, and Beyond (Review)

Conrad Rizal[1,2,*], Boris B. Niraula[2,†]

[1] *University of California, San Diego, La Jolla, 92093 CA, USA*
[2] *University of British Columbia, Vancouver, BC, Canada, V6T 1Z4*

When suitably alloyed, ferromagnetic-nonmagnetic (FM-NM) and ferromagnetic-ferromagnetic (FM-FM) alloys display remarkable saturation magnetization and magnetoresistance (MR). They also possess the ability to form well defined, unique micro and nano structures over a wide temperature range, and when prepared under closely controlled condition. This review aims to provide insights on how to synthesize macro and nano structures from the nano particles Co-Ag, Co-Cu, Co-Au, and Fe-Co alloys under controlled condition and explores magnetic and MR characteristics of thus synthesized micro and nano alloy structures - including giant MR, and saturation magnetization. Fabrication of these alloy based micro and nano structures was conducted using pulse-current deposition. Characterization was carried out using vibrating sample magnetometer, X-ray diffractometer (XRD), and rf-SQUID meter. XRD profiles and other characteristics of variously prepared nanostructures are compared in terms of particle size and lattice constant. Results suggest that both the increase in MR and saturation magnetization in FM-FM based alloys strongly depend on particle size and lattice constant in micro and nano structures.

This manuscript reviews the presence of a variety of MR effects in nano-structures of FM-NM alloys and it also investigates the relationship between saturation magnetization, alloy composition, and lattice constant, also referred to as crystallographic state of the constituent element, employing phase diagram. Results presented in this review suggest that these nano-structures can potentially be employed to create next generation of bio-magnetic devices for bio-medical and electronic applications due to the ease of fabrication and low cost associated with their preparation as opposed to presently available similar material used for biomedical application.

Keywords: Ferromagnetic alloys, GMR, Biosensor, Biocompatible Fe-Co, Microstructure, Saturation magnetization.

1. INTRODUCTION

A large number of new alloys in the form of composition-modulated structures such as nanowires, nanorods, and nanoparticles have been found to exhibit interesting electrical and magnetic properties - including giant magnetoresistance (GMR), super-paramagnetism, high saturation magnetization (M_s) as compared to traditionally synthesized similar alloys. And, in particular, these alloy based nano-structures and micro-structures exhibit interesting functional magnetic characteristics that varies with preparation conditions, chemical composition, layer thicknesses and deposition methods [1-21]. The properties of these nano and micro based structures, and in particular, properties of those ones that are fabricated under carefully controlled conditions, suggest that they can be employed in making a variety of devices including Hard drives for computers, MR sensors for automobiles, spintronics for magnetic memory, and biosensors for bio-nanomagnetic-based medical devices. However, it is not yet clear how and to what extent physical properties of these nano structured alloys can be manipulated by growth mechanism, layer thicknesses, composition, and it is for this reason this work finds its scientific merit and technological usefulness.

Depending on the way they are alloyed, Ferromagnetic alloys are classified into two broad categories:

i) Dispersed and Emulsified Ferromagnetic (FM) granules in non-magnetic (NM) material referred to as FM-NM alloys. These are best known for their GMR effect as a result of coupling between 4-*s* and 3-*d* electrons within the structure and the scattering of electrons at the interface that in turn depends on particle sizes and inter-particle distances.

ii) Dispersed and embedded granules in Ferromagnetic (FM) material, and they are referred to as FM-FM alloys. These are best known for their high saturation magnetization at room and low temperature.

The MR effect in FM-NM alloys can be either positive (in case if it increases with electrical resistivity) or negative (if it decreases with electrical resistivity) and this depends on metal type, alloy composition, electronic configuration of the metal used to fabricate it, and the physical structure – including on size and shape of particles used for their synthesis and inter-particle distance. The MR of the nano structure also depends on direction of applied field, *H*, and orientation of magnetic moment, *M*, with respect to the polarity of current, *I*, employed for deposition during its/their synthesis.

Six categories of MR have been discovered so far: (i) ordinary MR (OMR), (ii) anisotropic MR (AMR), (iii), giant MR (GMR), (iv) spin hall MR, (v) tunnel MR

(TMR), and (vi) colossal MR (CMR) [22]. MR effect significantly changes with changes in materials used and deposition mechanism. This paper briefly reviews the first three categories of MR that are more relevant to metals and alloys.

OMR effect, usually demonstrated by NM metals, is an increase of electrical resistivity. The resistivity is always positive in this case due to an external magnetic field, which is usually independently of its direction. It arises, especially in NM metals from cyclic motion of electrons due to the *Lorentz force*. Typically, the OMR effect in metals is proportional to the square of H, i.e., OMR $\propto H^2$, when the product of cyclotron frequency, ω_c, (ω_c is defined as $eH/2m_e$, where e and m_e are the charge and the mass of the electron, respectively) and relaxation time, τ, is much smaller than unity. This kind of effect is specifically exhibited by metals that do not possess spontaneous magnetization, such as Cu, Ag, Au, Mg, Zn, Cd, Ga, Ti, Sn, Pd, Pt. The effect is very small at applied H field below 1 kOe, however, it becomes very large at applied H fields over 1 kOe.
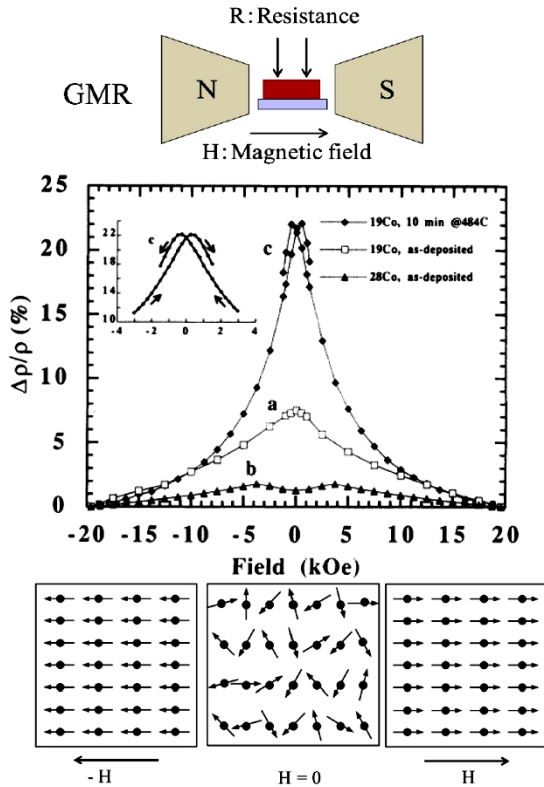

Fig. 1 – GMR effects in Co-Cu alloys: Reproduced with permission from [2]

Also, the transverse resistivity, $\rho_\perp$, i.e., the resistivity when $H \perp I$, is always larger than the longitudinal resistivity, $\rho_\|$, i.e., the resistivity when $H \| I$, though there is no unique theory to explain why this is the case. In addition, the magnitude of OMR is temperature sensitive. For example, the effect is much larger below room temperature, due to decrease in scattering of the thermal-phonon. For further information on OMR, readers are referred to [23, 24].

Unlike the OMR effect, the AMR effect, in which the electrical resistivity, ρ, can be positive or negative,

and it depends on the relative angle, θ, between the magnetization, M, and the magnitude and polarity of deposition current, I, employed for fabrication of these alloys. Electrical resistivity and AMR are related, and it is one of the most important and fundamental characteristic of 3-d transition metals and their alloys [12, 13]. AMR ratio is measured to evaluate the amplitude of electrical resistivity effect, and is defined as, $\Delta\rho/\rho = [(\rho_\| - \rho_\perp)/\rho_\|] \times 100 \%$, where $\rho_\|$ and $\rho_\perp$, represent, respectively resistivity for the $M \| I$ and $M \perp I$ [25].

Theoretically, the AMR ratio is derived by considering the effect of ρ and it can be due to the scattering of the s-d electrons. It is generally believed that the conduction electrons are scattered into localized d states in the presence of impurities or external factors such as applied H fields. Also, unlike s-electrons display, the d-state electrons, exchange field, H_{ex}, and s-d electron interaction, i.e., λLS, where λ is the s-d coupling constant, L is the orbital angular momentum, and S is the spin angular momentum, each expressed in 3-axes. Several theoretical models have been proposed to account for the AMR effect in metals and their alloys. Examples are the Campbell-Fert-Jaoul (CFJ) model [26] for weak ferromagnets and Malozemoff extended CFJ model [27], and, these are applicable for both weak and strong ferromagnets. Since a detail theoretical description of the AMR effect in metals and their alloys is beyond the scope of this review, interested readers are advised to read recent papers by Kokado et al. [25, 28].

As shown in Fig. 1, the giant magneto-resistance (GMR) effect, defined as $[\rho_{0(0,\,T)} - \rho_{(H,\,T)}/\rho_{0(0,\,T)}] \times 100 \%$, where $\rho_{(H,\,T)}$ and $\rho_{(0,\,T)}$ denote resistivity of the alloy at the demagnetized and magnetized states, respectively, was first discovered in Co-Cu granular alloys [2], soon after it was discovered in layered structures [29-31]. At the same time, GMR was reported in Co-Ag alloy system [3, 32]. This generated significant interests in new GMR granular material and, in particular, interest in pulsed-current electrochemical deposited FM-NM granular alloys is prompted by a few important considerations such as, possibility of fabrication of high quality granules at room temperature, possibility of deposition of alloy films at room temperature, fast granule growth rate, ease in operating electrochemical devices and possibility of having a high degree of control over deposition process [33-35]. For further information on the pulsed-current deposition, interested readers are advised to read previous papers by our research groups [6, 8, 10, 36-41].

Figure 1 shows H dependence of MR for three different Co-Cu alloys at $H = 20$ kOe and $T = 100$ K (a, b) $T = 10$ K (c), both at maximum ρ (that is at demagnetized state) and minimum ρ (magnetized condition). The inset (c) shows an enlarged view of the MR when the samples are in $H \| I$. It is believed that a maximum GMR is observed when all the particles in a sample are ferromagnetically aligned with the direction of applied H fields.

Unlike in multilayer, where geometrical parameter including layer thickness, defines the GMR effect, due to the heterogeneous nature of the granular alloys, the GMR effect in these are defined by factors such as par-

ticle size and particle size distribution, and their state and degree of magnetization (such as super-paramagnetic, SPM, and ferromagnetic, FM, i.e, non-SPM particles), as well as inter-particle distances.
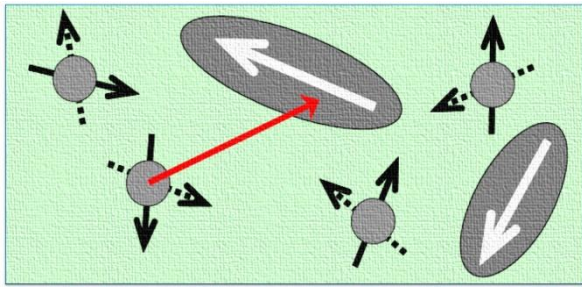
Fig. 2 – The GMR mechanism in the granular alloys: super-paramagnetic (circles) and ferromagnetic (ellipsoids) particles. Reproduced with permission from [42]

SPM particles are single domain magnetic particles, with d ≈ 3 to 50 nm, where M can easily flip its orientation under small changes in T, as given by *Néel relaxation time, τ_N,* which is equal to $\tau_0 \exp(KV/k_BT)$, where τ_0 is *attempt time,* and it usually lies between 10^{-9} and 10^{-10} seconds, K is the nanoparticle's magnetic anisotropy constant, V is volume, k_B is the Boltzmann's constant $\approx 1.38064 \times 10^{-23}$ J·K^{-1}, and T is the temperature [43, 44]. The $\sum M$ of the SPM in the alloy appears to be zero in average at $H = 0$.

Fig. 2 shows a schematic of a FM-NM granular alloy that consists of both SPM and non-SPM (FM) nanoparticles, imbedded in a non-magnetic (NM) matrix [42]. The arrows attached to each SPM granule indicates a random orientation and the fluctuation of M in alloy samples, as determined by their atomic composition, particle size, d, inter-/ intra-particle distance, t, and the density, δ, of constituent particles. Also, it is believed that the conduction electrons usually get polarized by the SPM nanoparticles and these can undergo multiple spin-dependent scattering depending on how its M are aligned with the spin of SPM particles [9, 45]. It means that the GMR of the alloy depends not only on overall size of these SPM particles but also on scattering of conduction electrons at the interface between the FM and NM particles [46]. When an H field is applied to the alloy, the M of the non-SPM particles (as indicated by long white arrows) rotate towards the applied H fields. Also, even at high H fields, the M of the SPM particles, however, are not fully saturated and stay at an angular position with respect to the direction of applied H fields. It is important to note that the SPM particles depicted in Fig. 2 using dotted arrows become SPM only above the blocking temperature, T_B; it is the temperature at which the magnetic moment of the SPM particle freeze to rotate, i.e., in this case the measured M will be equal to instantaneous M of the SPM. It implies that it is the temperature at which the transition occurs between the SPM and blocked state below T_B, and it, in turn, means that SPM are still ferromagnetic. It is generally believed that, below T_B, it is the critical diameter of the particles, d, that acts as a boundary between the SPM and FM particles.

Mathematically, the SPM particles can be measured in: i) Volume fraction, V_x in the alloy, whose value can vary anywhere between 0 and 1, and ii) Average particle diameter, $d = 2 \times r$, where r is the particle radius. Both V_x and r can be experimentally controlled by optimizing various deposition parameters such as, pulsed current width and height, and deposition conditions such as, electrolyte composition, T, pH, etc. These are further discussed in Section 2.1.

Let us first examine the effect of particle sizes on the GMR alloys. For simplicity let us assume that all SPM particles are of spherical shaped and can be calculated as, $N \cong 2V_x / d^3$, where N is the total number of particles. The average SPM particle separation, t, is given approximately as: $t = (2/V_x)^{(1/3)} \times d$. Note is to be made that t is crucial in determining both the magnitude of M and MR properties of any granular system. It in turn implies that both the V_x and d contribute to the magnetic interaction and interfacial electron spin-dependent scattering of the conduction electrons, and, thus, contribute to both the M_s and GMR. Using the surface (S) to volume (V_x) ratio, the total S of any SPM particles, can be given as, $S \cong 6V_x/d$, and is more accurate for uniformly distributed SPM particles [46].

The spin dependent MR effect has its origin on scattering of conduction electrons and it is yet another important characteristic of ferromagnetic multilayers that can be extended to the FM-NM alloys and nanoparticles, where the electron scattering strongly depends on the interface states between FM and NM grain boundaries. When mean free path of the conduction electrons becomes smaller than the diameter of the FM grains in the alloys or nanoparticles, the probability of electron scattering at the interface increases, resulting in a higher ρ in alloys. If we aim to define the spin orientation of 4-s conduction electrons for the magnetic particles (i.e., non-SPM particles) in parallel state (↑↑) (spin-up, ↑) or anti-parallel (↓↓) (spin-down, ↓) with respect to the direction of the M of these particles, for spin ↑ electrons, the contribution to its ρ becomes high due to higher rate / degree of scattering, while for spin ↓ electrons, the contribution to its ρ becomes low.

When one aims to define the ρ of the spin-up and spin down electrons, as ρ^+ and ρ^-, respectively, and the ρ of the magnetic non-SPM and that of the SPM particles, the total resistivity is given by, $\rho = \rho_{ns} + \rho_s$. Theoretical description of MR in alloys is beyond the scope of this review, and interested readers are referred to Ref. [46]. Experimentally, the ρ arising from the spin-dependent scattering can be controlled using external H fields.

It is also important to investigate how the GMR in FM-NM alloys and the saturation magnetization of the FM-NM alloys are linked to the atomic composition and crystal structure in the alloys and alloy based thin films. Equilibrium phase diagram of Co-Cu indicates that the solubility of Co-Cu solid phase at the eutectoid temperature, 422 °C, is 0.04, 0.10, and at 99.96 % Cu for ε-Co, α-Co, and Cu phases, respectively [36]. The Curie temperature of Co is 1121 °C and it decreases when Cu is added to it. Because of the small difference between the lattice constant of α-Co and Cu for both the super-saturated solution if prepared electrochemically [38] and for a single phase solid solution if prepared using high vacuum vapor deposition method [47].

In general, magnetic properties of Co-Cu alloys are closely related to micro-structure and atomic composition (at. %) of Co and Cu [48]. GMR of up to 4.0 % for the electro-deposited [49] and 6.3 % for the pulsed-current deposited Co-Cu alloy films has been reported at room temperature [38].

The equilibrium phase diagram of the Co and Ag shows that the metastable fcc-structure [50, 51] for a full composition range. The electro-deposited alloys can be precipitated to produce phase-separated fine particles at all composition range. They show a α-Ag structure for up to 85 % Co and a α-Co structure above it [7]. The room temperature GMR of up to 5.1 % has been observed for as-deposited Co-Ag alloys prepared using pulsed-current deposition [7]. The micro-structural and saturation magnetization properties are found to strongly depend on atomic composition of Co and Ag in alloys [52], and this aspect will be further discussed in Section 3.

As in the case of Co-Ag alloys, experimental evidence suggests that meta-stable Co-Au alloys can be grown below 420 °C [47]. The equilibrium phase diagram also shows that they are immiscible up to 420 °C. The maximum solubility of Co with Au at 996.5 °C is only 23 at. % [47]. Thus, instead of forming a solid solution, a suitable mixture of Co and Au can be made in equilibrium at room temperature using the pulse current electrochemical deposition method and when nano-sized particles are used. As is usual for most alloys, magnetic properties of Co-Au depend on film micro-structure and on composition ratios of Co and Au. A GMR value of up to 4.5 % has been reported for pulsed-current deposited Co-Au alloys [45].

A comparison between the OMR, AMR, and GMR effects shows distinctly intriguing and interesting characteristics in 3-d transition metals and their alloys. Unlike the OMR and AMR effects, the GMR effect is always negative, and independent of the direction of H and polarity of applied deposition current, I used (the GMR in FM-NM alloys is isotropic), and is qualitatively different from both the OMR and AMR effects [18, 46, 53, 54]. Likewise, the characteristics of the GMR in FM-NM alloys is significantly different from the OMR and AMR characteristics of NM metal and FM-NM alloys, and as well from that of the anisotropic GMR effects in FM / NM multilayers. The AMR in metal and alloys is attributed to the spin-orbit (s-d) interaction at $H = 0$ and the orientation of M with applied deposition current I at $H \neq 0$ whereas the GMR in alloys is considered to be due to the spin-dependent scattering (s-s or s-d) effect at the FM and NM granules interface.

Like the GMR effect in FM-NM alloys, the FM-FM alloys (e.g., Co-Fe, Fe-Ni, and Ni-Co), exhibit AMR effect and high saturation magnetization, M_s [55-57] in both layered and nano-particle based structures such as nanowire and nanoparticles. Although the magnitude of AMR is small, if alloyed appropriately, FM-FM alloys, especially the Fe-Co alloys, display a large M_s, which is usually well above the M_s of the individual ferromagnets at room temperature [8, 58]. The large M_s in these alloys make them very attractive for their applications in hospitals, for example, in early disease detection of chronic diseases. However, there are two

problems in Fe-Co alloys produced so far: one is that the grain sizes are larger than the sizes of the biomolecule cells and the other is that the maximum room temperature saturation magnetization, M_s, is still low, primarily due to the formation of oxide during the growth. These issues have significantly limited their use in biomagnetic sensing and drug delivery, for example. Furthermore, the relationship between the internal state of Fe-Co alloys and M_s has not yet been fully understood, and the questions as to how the M_s of these alloys can be enhanced, remains unanswered.

As in the case of FM-NM alloys, the M_s of FM-FM alloys is strongly linked to their microstructure, which in turn is related to their phase relationships they exhibit-including alloys of Fe-Ni, Ni-Co, and Co-Fe. The Fe-Ni phase diagram shows a solid solution of γ-Fe-Ni above 912 °C. Below 912 °C, pure γ-Fe exhibits a phase transition to the α-phase [59]. Ni-Co alloy systems exhibit complete solid solution in the α-phase temperatures range, including its solid-allotropic transformation temperature of α to ε (closed-packed hexagonal) phase. However, to date α to ε phase transition temperature boundary has not been established yet, because of the difficulties in achieving equilibrium at low temperature. Maximum solubility of Ni with Co is 5 at. % at 250 °C [60].

Between the three types of FM-FM alloys, the phase diagram of the Fe-Co alloy system has been extensively studied, especially in the temperature range of 400 to 800 °C. However, the phase diagram is not straight forward. What is interesting and important is that the α to γ transition as well as α and γ phase equilibrium extends to low temperature [61, 62].

As far as studies are concerned, most studies in this area are concentrated in enhancing M_s, by varying mixing ratios of these alloys. While it is known that 3d electrons are responsible for the high M_s in the Fe-Co alloys, a little attention has been paid to the investigation of relationship between degree of magnetization and the lattice constant, a. In addition, with the exception of the large M_s reported at low temperature, little progress has been made in improving the M_s of these alloys at room temperature.

It is a well-established fact that the physical properties (e.g., MR, M_s, a, optical properties, e.g., permittivity, ε, etc.) of both the FM-NM and FM-FM alloys discussed above to some degree depend on factors such as method of synthesis, materials used and their composition, substrate type when films are deposited, and the size and size distribution of the particles. It is to be noted that most FM-NM and FM-FM alloys reported in literature have been produced using methods such as non-equilibrium melt-spun [63], mechanical alloying [4, 6], high vacuum sputtering [64-68] and e-beam evaporation [69], and electrochemical precipitation methods [48, 70-79].

Pulsed-current deposition is an electrochemical precipitation method [79-82] that has added advantages over all the non-equilibrium and physical deposition methods. And, specifically, it is useful for the deposition of composition modulated FM-NM and FM-FM granular alloys with controllable granule size and shapes. And, what more is that intended results such

as controllable film thickness, growth rate, grain shape and size can be achieved using this method from a single electrolyte system, containing two or more elements, both at room and elevated temperatures, and it is this aspect of magnetic material that is the focus of this review. The beauty of this method is that by controlling the pulse height and pulse width, various compositionally modulated alloys and uniformly distributed nano particles can be produced in all kinds of shapes and geometries. This deposition technique comes with additional advantage such as ease of deposition and controllability, and it also offers the possibility of precipitating various immiscible and non-equilibrium alloys with a periodicity down to the atomic level [83-85].

The review is organized as follows: The first part starts with a brief background of MR in metals and in FM-NM alloys, taking consideration of how electrical resistivity and magnetism are inter-related, both at room temperature (293 K) and elevated (723 K) temperature. It is followed by a brief discussion on particle size distribution dependent resistivity / conductivity of the alloyed nano-structure and granular alloys, techniques used in producing granular alloys, exploration of their characteristics such as MR and magnetic measurements, and characteristics of alloyed microstructures fabricated using controllable electrochemical technique and under controlled deposition. It surveys published results, especially in the last 3 decades, and in particular on inter / intra-relationship between the magnetic properties such as M_s and MR, and lattice constant of alloys such as Co-Ag, Co-Cu, Fe-Cu, and Co-Au. In the second part, this review underlines the importance of FM-FM alloy and a special attention is paid to Fe-Co alloys. The relationship between the M_s and lattice constant reported in the recent works of Fe-Co alloys, prepared using controlled pulsed-current electrochemical method and its role in enhancing the M_s by means of control over grain size and grain size distribution, and about the possibility of obtaining well-ordered alloyed structures in atomic scale when electro-chemical pulse current deposition technique is employed. The review concludes with the summary, potential applications, and future prospects of ferromagnetic alloys.

2. PREPARATION, MEASUREMENT AND CHARACTERIZATION

2.1 Preparation and Composition Analysis

Because of its simplicity, low cost, and a high degree of possibility of control over deposition condition, Pulsed-current deposition technique is one of the most useful methods for growing metals and metal alloys on the atomic scale, using a single electrolyte and at room temperature. Although finding a suitable deposition condition is a challenging task, it is proven to be a promising method for producing magnetic alloys and films by having the possibility of control over deposition parameters. In addition, it shows several merits over galvanostatic method (constant-current), deposition using vacuum techniques such as e-beam evaporation, rf-sputtering, etc., and techniques that use elevated temperature for alloy deposition. Furthermore, it offers the opportunity of precision in making alloys on

an atomic scale. The electrical, magnetic, and microstructure properties can be easily manipulated by regulating the film composition, pulse amplitude, and pulse width. In addition, no extensive training is required to synthesize nanostructured alloys. Grain sizes of the alloys are optimized by the pulsed-current deposition method, and are found to be smaller and finer than those grown using the vacuum evaporation and constant-current methods. These benefits make pulsed-current deposition one of the most preferred alloys deposition methods, when producing high quality alloys in the form of layered films, nano-wires or nano-pillars and nano-particles.

Fig. 3(I) shows a typical pulsed-current waveform where, J is the current density (A/m²), t is the deposition time (ms), T_A is the time, during which the current is applied, and T_B is the time, during which no current is applied. Similarly, J_A is the current density during the period of T_A, J_B is the current density when no current is applied, and J_{avg} is the average current density. Note is to be made that by adjusting the deposition time and the amplitude of the current density composition modulated alloys of two or more elements with various compositions and thicknesses can be prepared using this method.

Fig. 3(II) on the top shows a schematic for the generation of pulsed-current. It consists of four major parts: a microcomputer, a D-A converter, a regulator (a constant-current circuit.), and an electrochemical cell. As shown in this Figure, a digital signal is fed through the programmable microcomputer which in turn feeds the D-A converter. The out going analog signal from the D-A converter is then fed to the regulator. The output signal from the regulator is then passed into the electrochemical cell, where the deposition takes place at the electrode that acts as a substrate as well. As shown in the Figure, it consists of a single electrolyte with two or more metal elements in it. Fig. 3 (III) is the enlarged view of the electrochemical cell consisting of metal A and B in a single electrolyte.

Note: all the FM-NM and FM-FM alloys reviewed in this paper were prepared using the pulsed-current deposition method. The principle of pulsed-current deposition for the alloy is similar to the principle of pulsed-current deposition for the multilayers we reported earlier [10, 39, 80, 87] except that the pulse current width (i.e., deposition time) for the alloy deposition is much smaller (up to 0.01 ms) as opposed to pulse current width used for the multilayers [88].

Fig. 3 (IV) shows the principle of pulsed current deposition where the x-axis is the electrode potential (corresponding to the current density), the *y*-axis is the deposition time, and the layer thickness of the film is related to deposition time. The principle of composition modulated alloy deposition is as follows:

At an applied potential V_A, the metal A is deposited but at a potential $V_{(A + B)}$, an alloy of metals A and B is deposited instead. By changing the current density (potential) alternately between these two values, any combinations of composition modulated alloys and nano-particles can be produced. The beauty of this process is that by controlling the pulse amplitude and pulse width, one can produce a variety of combinations of alloys, at an atomic scale, from a single electrolyte and at room
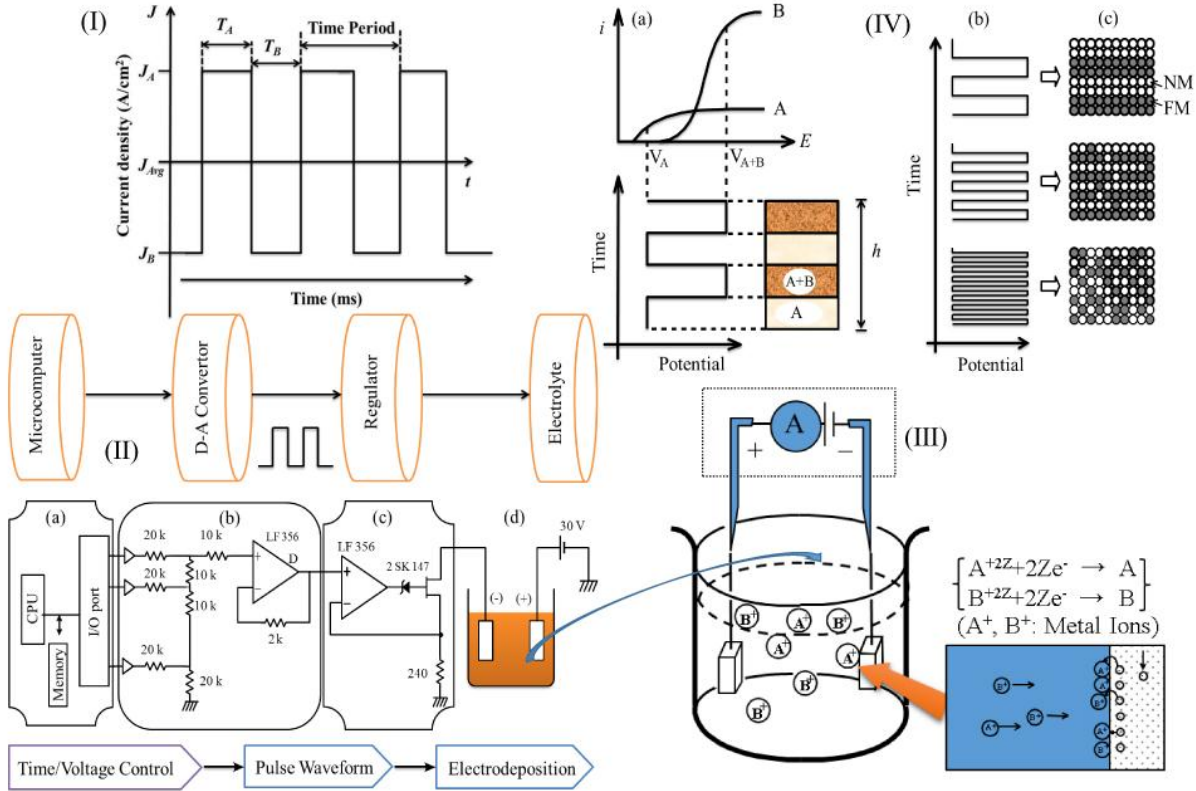
Fig. 3 – (I) Pulsed-current wave shape, (II) An electronic circuit diagram for generating pulsed current deposition, (III) Enlarged view of the electrochemical cell, and (IV) Principle of the pulsed-current deposition showing pulsed current wave shapes with different deposition time and corresponding alloys [80, 86]

Table I – Electrochemical parameters and deposition conditions for the FM-NM alloys. Reproduced with permission from [7, 90]

Co-Ag		Co-Cu		Fe-Cu		Co-Au	
Constituents	**g/L**	**Constituents**	**g/L**	**Constituents**	**g/L**	**Constituents**	**g/L**
$CoSO_4.7H_2O$	5-16	$CoSO_4.7H_2O$	28-39	$FeSO_4.7H_2O$	2-16	$CoSO_4.7H_2O$	1-10
$AgSO_4$	0.1-5.5	$CuSO_4.5H_2O$	15-25	$CuSO_4.5H_2O$	2-16	$AuK(CN)_2$	15-25
$Na_3C_6H_6O_7.2H_2O$	76	$Na_3C_6H_6O_7.2H_2O$	76	$Na_3C_6H_6O_7.2H_2O$	76	$Na_3C_6H_6O_7.2H_2O$	76
$Na_2SO_4.10H_2O$	4	NaCl	2	-	-	NaCl	2
pH	9.5	pH	6.0	pH	5.0	pH	4-6
J (mA/cm²)	1-10	J (mA/cm²)	2-10	J (mA/cm²)	5-15	J (mA/cm²)	1-10
Temperature (°C)	85	Temperature (°C)	25	Temperature (°C)	25	Temperature (°C)	50

temperature. This method offers the possibility of simultaneous co-deposition of different metals, which are normally immiscible, and on a single substrate from a single aqueous solution, and it is a main advantage of the pulsed-current deposition technique over others.

The number of metal atoms deposited on the substrate is proportional to the amount of used electricity in accordance to Faraday's law. Using this law, the nominal thickness, h, of the deposited alloy is given by,

$$h = \frac{A_w \times \eta}{n \times F \times \delta \times S} \int i \times \partial t = \frac{\eta \times A_w \times I \times t}{n \times F \times \delta \times S}, \quad (1)$$

where t is the deposition time, A_w is the atomic weight of the material, η is the cathode current efficiency and its magnitude is unity at ideal deposition condition, δ is the density of the deposited material, J is the current density (expressed as I/S, where I is the current and S is the surface area of the sample), n is the valency of the metal, and F is the Faraday's constant and is equal to 96500 C [89]. The cathodic current efficiency, η was chosen between 0 and 1, depending on the type of electrolytes used. The t, J, and η are the three most important parameters that determine the amount of constituent materials being deposited. The pulsed-current deposition method discussed here can be exploited to deposit alloys and nano-wires with complex geometries that are usually not possible via sputtering, molecular beam epitaxy, or e-ion beam evaporation methods.

By controlling the electrode potential (current density), the deposition times, t, and the constituent elements in the electrolyte, both FM-NM and FM-FM alloys in various composition and thicknesses can be produced. Note is to be made that the grain sizes of alloys

prepared using pulsed-current deposition are found to be smaller and finer than that of the grains produced using constant-current, potentiostatic or high vacuum deposition methods [80, 89]. The wide range of electro-chemical parameters and deposition conditions that have been used in fabricating FM-NM alloys reviewed in this paper are given in Table I [7, 10, 90].

Table II – Electrodeposition parameters and deposition conditions for Fe-Co alloys. The composition of the alloy was controlled by changing the Fe and Co ion concentration in the electrolyte [8]

Constituents	m (g/L)	Parameters	Quantity
$CoSO_4.7H_2O$	0-56	J (mA/cm²)	1-10
$FeSO_4.7H_2O$	0-50	Times (s)	0.2-10
$Na_3C_6H_5O_7.2H_2O$	76	T (°C)	20
NaCl	2	pH	6

The Fe-Co alloys reviewed here were prepared from sulphate based electrolyte using pulsed-current deposition and by reducing the deposition times to nanoseconds. The detail deposition parameters and deposition condition are given in Table II [8].

The composition of the alloy was also determined using a Flame emission and atomic absorption spectrometer. In order to accurately characterize the composition of the alloy, usually the analysis was carried out for five different standard solutions of the same material, and then the obtained data was fitted using the linear regression analysis.

2.2 MR and Magnetic Measurements

Magnetoresistance is an important material property, especially, of layered nanostructures and this can be measured using multiple techniques – including a four-probe contact method. Magnetic field, H acts as a probe in this technique and the H field can be applied to the sample substrate either in-plane parallel (∥) to the direction of current, I being applied to the sample substrate or in-plane perpendicular (⊥) or perpendicular-to-plane (⊥) to the sample and it can be achieved by varying the relative direction between the H and I in a field swept from ± H.

Resistivity was measured using two-point probe and four-point probe methods at room temperature and in the presence of both in-plane or out-of-plane H fields and in the presence of current I, in four different configurations as described below:
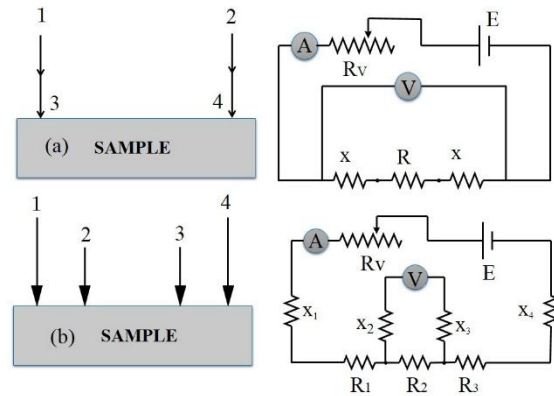
i) Two-point-probe method: As shown in Fig. 4(a), In the two-point-probe method, both the current, I, and voltage, V, are measured using two linearly aligned probes attached to the two ends of the surface of the sample. The I is passed through terminal 1 and 2, and the resulting V is recorded. The total V across the connector is the sum of the resistances of the alloy and the contacts. At low I, this V is linearly proportional to the I, accordingly to Ohm's law, and is given as,

$$V = (R + 2 \times x) \times I, \qquad (2)$$

where $R + 2x$ is the sum of alloy and contact resistances. A two-point I-V measurement method is only suitable for high resistivity (greater than 1 M Ω/m²) materi-

al, i.e., when the contact resistances are negligible as compared to the sample resistance.

A problem with the standard two-point I-V measurements is that the measured total resistance includes contributions from both the sample and connector-sample contacts (resistances are in series and, therefore, sum with the sample resistance). For low resistivity materials, this method can yield erroneous results because the contact and spreading resistance can vary significantly. In many cases, contact resistances are significant and must be distinguished from the sample resistance. Materials that do not exhibit ohmic I-V characteristics, differential conductance, dI / dV, is used to determine the resistivity. Only DC measurement is discussed here. The challenge associated with the two-point probe method can be overcome by using the four-point probe method.

Fig. 4 – Schematic of (a) two-point probe and (b) four-point probe circuits

ii) Four-point-probe method: As shown in Fig. 4(b), The four-point-probe method is best suited for measuring low electrical resistance, usually in nΩ ranges. In this method, the I is passed across two external probes and the V in the sample is recorded using two internal probes. The measured V is, therefore, the voltage across the sample with no current flowing through the contacts. It means that there is no potential drop in the connecting wires as well as at the connector-sample interface. As a result, the measured resistance reflects the actual sample resistance. For a four-point probe contacts, with two current probes 1 and 4 and two voltage probes 2 and 3, and an equivalent electrical circuit, with R_v is a variable resistor, R_1 and R_3 are the contact resistances, R_2 is the actual alloy resistance, E is the drive potential, and x_1, x_2, x_3, and x_4 are the probe resistances. The current flowing through the circuits is given by,

$$I = E / (x_1 + x_4 + R_1 + R_2 + R_3 + R_v) \qquad (3)$$

The voltage, V across the sample is given by,

$$V = E \times R_2 / (x_1 + x_4 + R_1 + R_2 + R_3 + R_v) \qquad (4)$$

Upon expressing the I and V relationship using Ohm's law, we obtain,

$$R_2 = 1/G_2 = V/I$$

The advantage of using the four-point probe meas-

urement is that the measured alloy resistance does not include any probe resistance (that is all the contributions from all contact resistances are eliminated) and, therefore, minimizes errors in the MR measurement. The actual resistance of a sample is the ratio of the voltage drop V and the current I passing through the sample. From the value of the I flowing through the sample, the distance between the voltage probes, and the cross-sectional area of the sample, the ρ of the sample can be determined.

The effects of layer thicknesses and compositions on the room temperature magnetic properties, e.g., saturation magnetization, M_s, remnant magnetization, M_r, coercive force, H_c, and anisotropy constant, K_u, were all studied using a vibrating sample magnetometer (VSM). As shown in Fig. 5, given a magnetic dipole with moment, M, lying along the x-axis, and vibrating with an angular frequency, ω, and the amplitude of vibration, 2a at a point $A(x, y, z)$ in the pickup coil along z-axis (normal to the sample surface), the induced voltage at $A(x, y, z)$ is given as [86]: $V_0 = (3 \times N \times S \times x/2r^5) \times a \times f \times M$, where $f = \omega/2\pi$ and is proportional to the amplitude of M, S is the surface area, N is the number of turns of the detection coil, and V_0 is the induced voltage at $A(x, y, z)$. If both a and f are kept constant, the induced V_0 is directly proportional to the M_s of the alloys. This principle is the basis for the magnetization measurement in most ferromagnetic alloys. Prior to the measurement, the VSM was calibrated using standard sample with a known M_s. For detail information on magnetic characterization of FM using VSM readers are referred to Refs. [91, 92].

The superconducting quantum interference device called rf-SQUID magnetometer is extremely sensitive to grain interactions in alloy and it is a useful tool for investigating magnetic properties, especially of superparamagnetic (SPM) material such as granular alloys, and this is usually achieved by means of zero-field-cooled (ZFC) and field-cooled (FC) magnetization measurements [9, 45]. Blocking temperature, T_B derived from ZFC curves are of special significance in this case; and the mean FM grain size is estimated as, $K_A \times V = 25k_B \times T_B$, where K_A is the magnetic anisotropy constant for fcc-Co, V is the upper limit volume of super paramagnetic grains (assumed spherical for simplicity) corresponding to the blocking temperature T_B (it is the temperature below which the magnetization will be stable), and K_B is the Boltzmann's constant. The coefficient of 25 comes from a measurement time of 100 seconds and it is roughly the time required to experimentally measure remnant magnetization, M_r, which is also the relaxation time over the energy barrier $k_B \times T_B$.

The particle size is usually determined using temperature dependent magnetization curve. Other devices that have been widely used for the magnetic characterization at room, high, and low temperatures are magnetic force magnetometer (MFM), physical property measurement systems (PPMS), etc., and these are left out for the future review.

2.3 Microstructure Characterization

Crystallographic orientation of the samples was analyzed using an X-ray diffraction (XRD) technique. The XRD was made of Cu-Kα based diffractometer of 60 kV
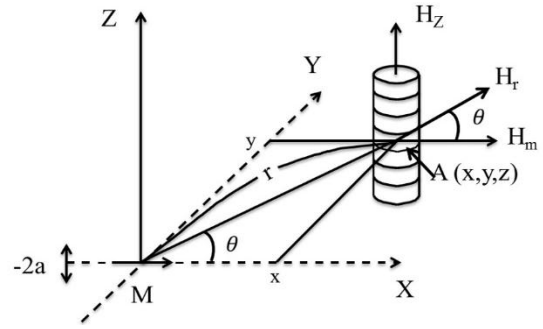

Fig. 5 – Schematic of measurement principle of M using a vibrating sample [86]

and 200 mA was used to obtain X-ray diffraction patterns [93, 94]. From these diffraction patterns, a detail information on the atomic makeup of the alloys and granules / particle sizes were also estimated from these diffraction patterns using Shearer's relation [93].

The condition for constructive interference to occur is given by Bragg's relation $2d \times \sin\theta_B = n \times \lambda$, where θ_B, is the Bragg's diffraction angle, d is the plane spacing, n is the order of reflection, and λ is the wavelength of radiation, which is 0.15406 nm for Cu-Kα radiation.

The size of particles and granules on those alloy based structures was estimated from these X-ray diffraction patterns using Shearer's relation as, $t = 0.9 \times \lambda/(B \times \sin\theta_B)$, where t is the diameter of the particle, B is the full-width-half-maximum of the diffraction peak, and θ_B is the Brag's diffraction angle. Given the value of d (plane spacing) and crystallographic plane $<hkl>$ which can be obtained from the *American Society of Testing of Materials table*, the lattice constant, a, of alloy granules / particles was estimated. For the characterization of alloys that are not crystalline, a low-angle X-ray scattering method is usually employed with powerful synchrotron or high-intensity laboratory sources.

Fig. 6(a) shows XRD patterns of the samples of Co-Cu and Co-Ag and (b) of Co-Au alloys. These were prepared using pulsed-current deposition method under controlled condition. As shown in the Figure, the alloys showed strong fcc-Ag, fcc-Cu and fcc-Au patterns for all the FM-NM alloys. The lattice constant, a, calculated from Fig. 6(a) is plotted as a function of alloy composition in Fig. 6(c). In the case of Co-Cu alloys, the a calculated from the diffraction angle of fcc-Cu decreases linearly with increasing Co concentration, and this trend suggests that samples examined in this case follow *Vegard's law*, which is a linear dependence of a with Co concentration / fraction / composition.

On the other hand, the fcc-a of Co-Ag alloys, did not vary with the Co composition / fraction / concentration. Note is to be made that the a of the Co-Ag alloy matches closely to patterns usually shown by bulk fcc-Ag. Similarly, the fcc-a of alloys calculated from the diffraction angle matches closely to the pattern usually shown by bulk fcc-Co (not shown here). It suggests that the a of the fcc-Ag is not affected by the presence of Co atoms in these alloys.

Based on these observations, it can be concluded that Co and Ag did not form any solid solution in these
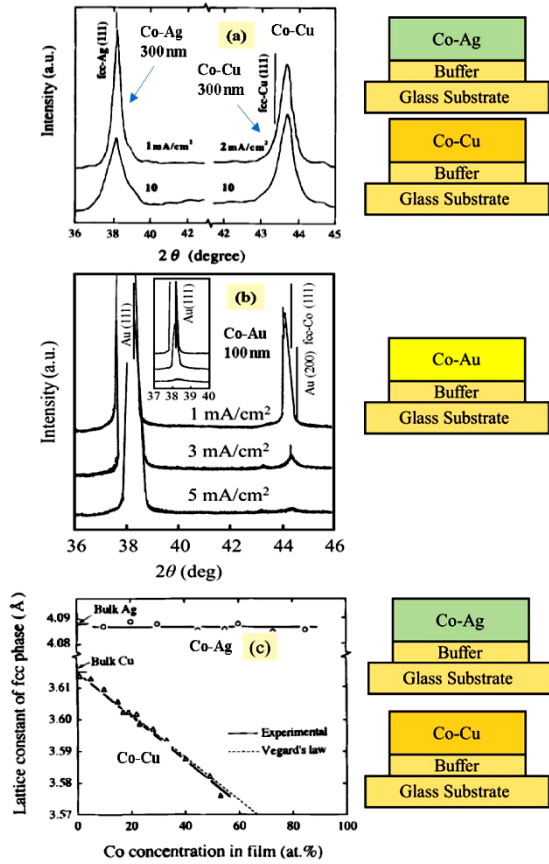
Fig. 6 – (a) X-ray diffraction patterns for Co-Ag, Co-Cu, and (b) Co-Au alloys prepared at different deposition current densities: (a) and (b) Reproduced with permission from [7]
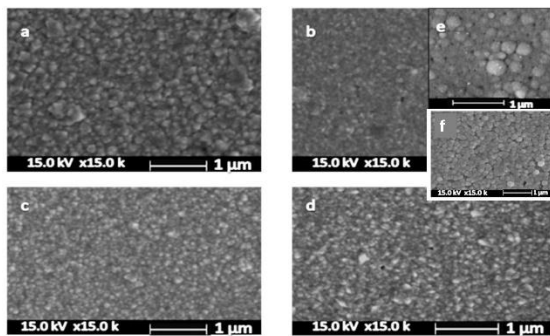

Fig. 7 – The SEM images of the Co-Au alloys prepared using pulsed-current deposition technique at the current density of (a) 1, (b) 3, (c) 5.5, and (d) 7 mA/cm². The inset shows enlarged SEM image for as-deposited alloys at (e) constant dc current and (f) pulsed-current, each deposited at 3 mA/cm². Reproduced with permission from [95]

alloys, which is in line with the phase diagram of Co-Ag alloys that show very low miscibility of Co-Ag [96], compared to the phase diagram of the Co-Cu [97] that shows good miscibility. It is to be noted that the atom size difference is greater for Co-Ag than for Co-Cu, and this can be a crucial factor in defining miscibility of metals in alloy samples. Despite the miscibility mis-matches the results presented here suggested strong fcc-texture for all FM-NM alloy samples examined here.

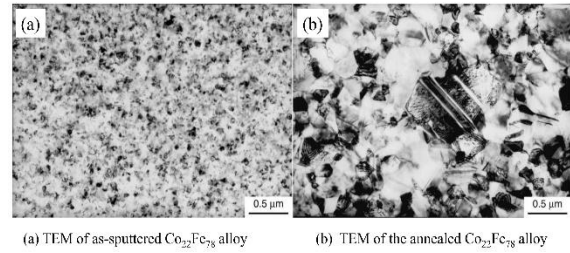To accurately extract information on the layer thicknesses, and surface / interface roughness parame-

ter,

Fig. 8 – TEM images of (a) as-deposited (b) annealed $Co_{22}Fe_{78}$ alloy (It is shown here to depict the effect of annealing on the particle sizes). Reproduced with permission from [62]

the experimental data can be analyzed using *GenX* [98] where model samples are defined using Python. More information on both the low-angle X-ray reflectivity and high angle X-ray diffraction analyses of ferromagnetic nanostructures will be available soon [99].

Fig. 7 shows scanning electron microscopy (SEM) images of Co-Au alloy samples and these were prepared using pulsed-current deposition. Samples deposited with different magnitude of deposition I are compared: (a) 1 mA/cm², (b) 3 mA/cm², (c) 5.5 mA/cm², (d) 7.5 mA/cm [95]. The inset shows SEM image of alloys prepared using constant dc current (e) whereas (f) was deposited using pulsed-current, each at $J = 3$ mA/cm². The optimum J and the off deposition times that gave the most uniformly distributed particle size are found to be 3 mA/cm² and 1.5 s, respectively.

Fig. 8 shows transmission electron microscopy (TEM) images of the as-deposited and annealed Fe-Co alloys [62]. The as-deposited alloys showed a very fine Fe-Co grain of very close size distribution that is centered at around $r \approx 50$ nm. Upon annealing at a temperature 400 °C, a phase separation into $\alpha + \gamma$ duplex structure is observed with the increase in particle size to 200 nm, and this increase is 4 fold compared to the particle size of the as-deposited ones.

3. EXPERIMENTAL SURVEY : FM-NM ALLOYS

The MR of FM-NM alloys is dependent on the way they are synthesized and alloy composition as confirmed by various previously published results [4, 8, 10]. As far as pulsed-current deposited FM-NM alloys are concerned, it is found that these possess some remarkable MR characteristics – including MR that is comparable to that of or larger compared to those prepared using multilayer non-equilibrium technique and high vacuum evaporation method. This can be due to the fact that pulsed current deposition technique produces FM granules of highly uniform nature in term of size distribution and shape. The electrochemical parameters and deposition conditions for these FM-NM alloys are shown in Table I (see, Section 2.1).

Fig. 9 shows MR for the as-deposited nanostructured Co-Ag, Co-Cu, Fe-Cu, and Co-Au alloys deposited at different deposition current density, J (A/cm²), and deposited from solutions of different chemical composition (at. %). The effect of deposition J on MR, as reported by Zaman et al. [7], (top) suggested that the MR of Co-Ag alloys is directly related and ef-

fected by deposition *J*. Co-Au samples studied by us showed similar results [10] (middle), whereas the MR of the Co-Cu and Fe-Cu [7] did not show any appreciable effect with changing deposition *J*.

In the as-deposited state, the alloys showed a maximum MR of 1 % at a $J = 1$ mA/cm² (Co- Ag), 0.8 % at a $J = 2$ mA/cm² (Co-Cu), 0.2 % at a $J = 1$ mA/cm² (Fe-Cu) and 1.4 % at a $J = 1$ mA/cm² (Co-Au). On increasing the current density, the MR increased to 5 % at $J = 10$ mA/cm² in case of Co-Ag, and 4.0 % at $J = 5$ mA/cm² in case of Co-Au, and these were carried out at room temperature and under a H field of 21 kOe.

Interestingly, the MR of the Co-Cu and Fe-Cu alloys did not change with the increase in deposition current densities. The MR of Fe-Cu is always found to be the smallest (below 0.5 %) of all the alloys reviewed here, irrespective of the increase of deposition current density [6], and this result is different from the MR of the mechanically grown alloys by Ikeda et al. (MR = 1.7 % at 70 at. % Cu) [4]. On annealing Co-Cu based alloys for 1 hour at 450 °C, however, its MR increased to 6.3 % and that of Fe-Cu also increased slightly. On the other hand, the MR of the Co-Ag alloys decreased appreciably, and this trend was more appreciable especially in those samples that were prepared at much higher current densities, (see Fig. 9 (bottom)).

It needs to be noted that much like those of Co-Ag alloys, the MR of Co-Au alloys deposited using pulse current slightly decreased upon annealing these at 400 °C for 30 minutes. This suggested that annealing helps produce alloy particles of optimum size and shapes and as a result these alloys display increased MR. These results in turn suggest that Co particles of favorable size distribution and shape are the requirement for obtaining a larger MR response in Co-Cu and Co-Au alloys but not in Fe-Cu alloys for which particle size distribution did not change with applied deposition pulsed current density.

To understand the nature of MR exhibited by various alloys, Ueda and Zaman et al. [6, 38] studied *H*-dependent MR responses extensively on Co-Cu, Co-Ag, Co-Au and Fe-Cu. Their results suggested that MR did not saturate even at $H = 21$ kOe and it is in agreement with the first report of GMR in FM alloys by Berkowitz et al. [2]. The same was the case for the M-H curves. However, for the mechanically alloyed Co-Cu [4], the *M-H* curves saturated at or below $H = 4$ kOe , suggesting that these alloys precipitate differently depending on how they were prepared [4].

It is generally believed that upon annealing, the MR of the electro-deposited Fe-Cu alloys decreased and the *M-H* curves showed a prominent hysteresis (not shown here). Clearly, this suggests that in the as-deposited state, these alloys were solid solution type and annealing resulted in phase separation of bcc-Fe and fcc-Cu particles, and it is similar to the phase separation of the Co-Cu alloys.

Fig. 10 (top) shows result from rf-SQUD meter. Using this technique experiments were conducted both at zero-field cooled (ZFC) and field-cooled (FC) states. These results also suggest that size distribution of alloy particles changes with change in deposition conditions. It in turn means that the mean particle sizes of the

electro-deposited Co-Ag alloys are strongly dependent
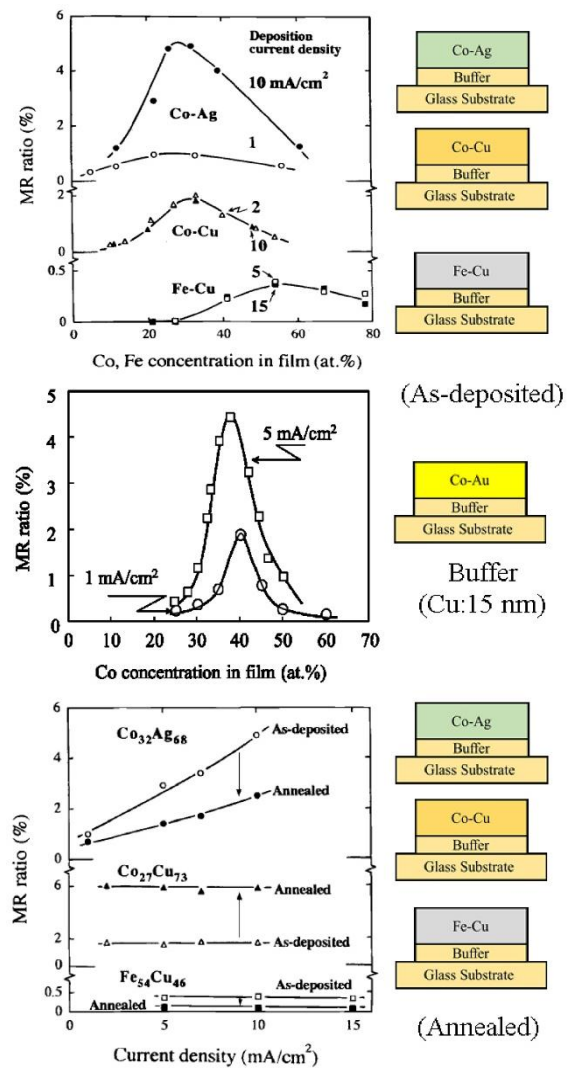
Fig. 9 – (a) Plot of MR versus composition of Co in Co-Ag, Co-Cu, and Fe-Cu alloys at different deposition current densities (top). Reproduced with permission from [7]. MR vs composition of Co for Co-Au alloys (middle). Reproduced with permission from [45]. MR versus composition for the annealed Co-Ag, Co-Cu, and Fe-Cu alloys (bottom). Reproduced again with permission from [7]

on deposition current density [7]. For example, the mean particle sizes of the Co as calculated using rf-SQUID meter result suggested production of smaller particles at higher current densities. As shown in this Figure, the Co-Ag alloys were deposited at 10 mA/cm², and these showed a broad peak at about 120 K and a particle size distribution centered to about ≈ 10 nm.

It is thus, concluded that the larger MR displayed by Co-Ag alloy when deposited using a higher applied deposition current *J* of 10 mA/cm² in Fig. 9 is considered to be due to production of optimum sized alloy particles. From the ZFC curve of the Co-Cu alloys that was grown at $J = 2$ mA/cm², a peak is observed at about 90 K, and these ZFC peaks suggested that fine particles of ferromagnetic Co phases may have been precipitated. These precipitated ferromagnetic Co phases, however, are not necessarily a single Co phase. Similar results have been

observed for the Co-Cu alloys prepared using mechanical alloying as suggested by Ikeda et al. [4].
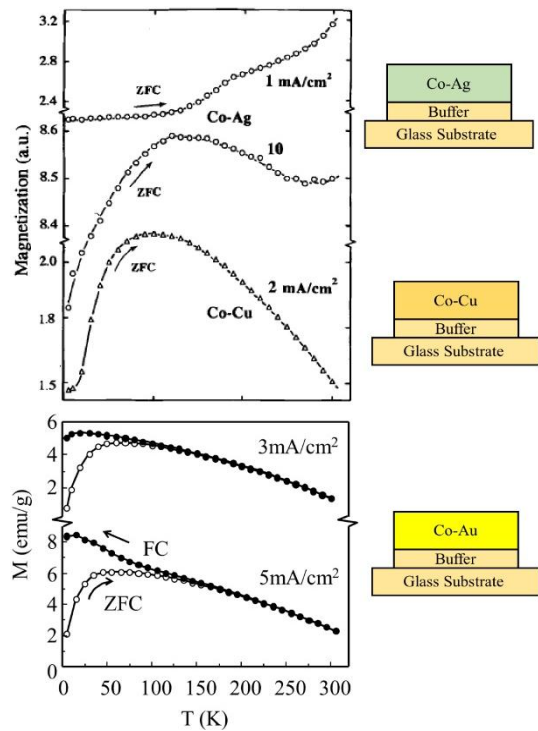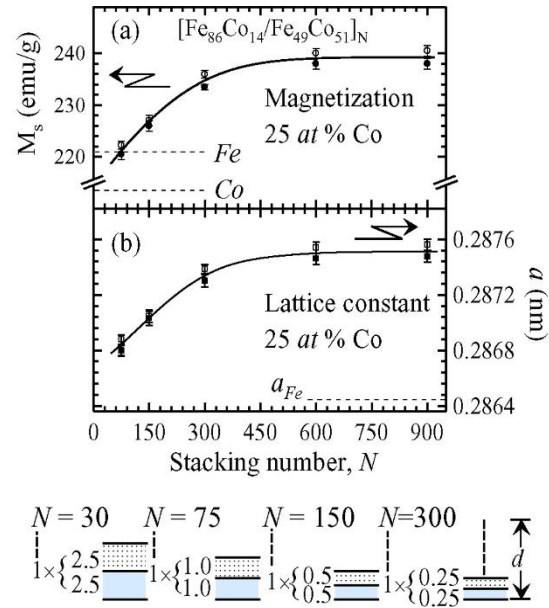

Fig. 10 – The temperature dependence of M_s for the Co-Ag, Co-Cu, and Co-Au alloys. Reproduced with permission from [90, 45]

As depicted in Fig. 10, Pulsed-current deposited Co-Au alloys showed that the size of the deposited particles strongly depend on applied current density for their deposition. Fig. 10 (bottom) shows the ZFC and FC curves for Co-Au alloys deposited at 3 and 5 mA/cm², respectively. The alloys deposited at 5 mA/cm² exhibited smaller particle sizes and the MR of 4.5 %, larger than the MR exhibited by alloys produced by deposition current of 1 and 3 mA/cm². It is thus believed that the small Co grains present in Co-Au alloys deposited at $J = 5$ mA/cm² are responsible for larger MR values exhibited by these alloys. These results are consistent with results reported by Guo et al. [75] where the

Fig. 11 – A relationship between Ms and a for the bcc-Fe-Co alloys. The composition deposited alloys shown in the bottom inset, were produced using a single electrolyte. The alloys were produced at room temperature without stirring. The composition in the deposited alloy was optimized by changing the deposition condition, chemical composition in the electrolyte, and deposition times, as listed in Table II [8]

grains with size range of 1.0-3.3 nm have been successfully dispersed in a matrix of Au. These results are somewhat analogous to the results of the Co-Ag alloys reported earlier [7]. Note is to be made that since the MR did not change appreciably with the composition and / or annealing, no low temperature investigation was carried out for Fe-Cu alloys.

It is a well-known fact that Co and Fe based FM granular alloys have dominated most research in soft magnetic material, and are currently considered the most important alloys, specifically for biomagnetic applications. Typical FM-NM alloys include Co-Au [45], Fe-Au [102], Co-Ag [11, 69], Co-Cu [38], Fe-Cu-Ni [39, 103], Fe-Ni [104], Co-Pt [105]. Table III lists the GMR effect in FM-NM Co-Cu, Co-Ag, Co-Au, and Fe-Cu

Table III – Comparisons of MR in various FM-NM alloys produced using both chemical and physical methods. (Only the representative works on pulsed-current deposited alloys are listed here.)

Alloys	Composition	Methods	Temperature	Field	MR	Ref.
Co-Cu	$Co_{19}Cu_{81}$	Sputtering	10 K	20 kOe	22 %	[2]
Co-Cu	$Co_{20}Cu_{80}$	Sputtering	5	20	17	[35]
Co-Cu	$Co_{10}Cu_{90}$	Melt-spun	300	6.5	11	[100]
Co-Cu	$Co_{70}Cu_{30}$	Pulsed-current	300	11	6.2	[36]
Co-Ag	$Co_{70}Ag_{30}$	Pulsed-current	300	10	9.1	[7]
Co-Au	$Co_{25}Au_{75}$	Pulsed-current	300	1	4.6	[9]
Co-Au	$Co_{15}Au_{85}$	Arc Melting	5	20	28	[101]
Fe-Cu	$Fe_{30}Cu_{70}$	Sputtering	5	20	9.0	[3]
Fe-Cu	$Fe_{70}Cu_{30}$	Mech. Alloying	300	4	1.5	[4]

alloys produced using sputtered, melt-spun, mechanically alloying, and electrochemical method, and these results have been reported elsewhere [2-4, 35, 100, 101]. For comparison it also lists the GMR effect of the FM-NM granular alloys produced and studied by us [7, 9, 36, 41]. Note is to be made that some of these were deposited on plastic substrates using pulsed-current deposition method. The list is not intended to give a complete overview, instead it is an attempt to cite only the representative works on pulsed-current deposited alloys.

The results also suggested largest room temperature GMR effect of up to 6.2 % and 9.1 % for the pulsed-current deposited Co-Cu and Co-Ag alloys, respectively. Previously published works have demonstrated that composition modulated alloys prepared using pulsed-current deposition method show GMR values that are comparable to or larger than the GMR values reported for multilayers and granular alloys [103]. This also suggests that pulsed-current deposition is best suited when it comes to producing nano-structured magnetic alloys with uniformly distributed particles and these demonstrate much larger MR effects compared to similar alloys prepared using other methods.

4. EXPERIMENTAL SURVEY : FM-FM ALLOYS

Ferromagnetic-ferromagnetic (FM-FM) Ni-Co [106], Co-Fe [8], [57] and Ni-Fe [104] alloys and $Fe_{16}N_2$ ferromagnets [19, 107] are remarkable materials because of their giant saturation magnetization, M_s and good AMR effects at room temperature [108-110]. Among the Ni-Co [106], Co-Fe [8, 57] and Ni-Fe [104] alloys, when appropriately alloyed using pulsed-current deposition method [8], Co-Fe alloys show the highest room temperature M_s, which is much higher as opposed to M_s of its bulk counterparts, prepared using other deposition methods and of the individual elements from which these alloys are made. Higher M_s is one of the main requirements for making ultra-fast and ultra-sensitive magnetic sensors from alloys, and is the subject of this review. Likewise, $Fe_{16}N_2$ is important ferrimagnet as it shows a giant magnetic moment, which is as high as 290 emu/gm at low temperature [111-114]. Materials with room temperature M_s exceeding 300 emu/gm can potentially be useful such as in making bio-magnetic sensors and in drug delivery and magnetic imaging. Reviews on $Fe_{16}N_2$ and other metallic biomaterials that have great potential for future applications are reported elsewhere [107] and is not considered here.

Fig. 11(a) shows relationship between M_s, and *lattice constant*, *a*. The *a* is plotted against number of stacks (bilayer number), *N*. The bilayers were alternately stacked bcc-$Fe_{1-x}Co_x$ alloys and these were also produced using pulsed-current deposition method. As shown in this Figure, the alloys exhibit increase in M_s with *N*, and reaches 240 emu/gm at room temperature as *N* was increased to 900 and at 25 at. % of Co. Fig. 11(b) shows a relationship between *a* and *N* for Fe-Co alloys. As depicted, *a* increases almost linearly with *N*. It indicates that the lattice expands with the increase in *N*, a result that is very similar to that was published in Ref. [108]. The increase in *a* with *N* is attributed to the elastic strain and magneto-volume ef-

fect. The increase in M_s with N in Fig. 11 clearly suggests that the solid solution of Fe and Co exists, i.e., Fe and Co miscible metals on atomic level, giving rise to an enhanced saturation magnetization. The trend of increasing magnetization is very similar to the trend of increasing lattice constant and this phenomenon is consistent with the results obtained from empirical methods [115]. This is an exceptionally important relationship and it can probably be attributed to enhancement in ordering of the bcc-Fe-Co alloy particles in atomic level.

5. SUMMARY, POTENTIAL APPLICATIONS, AND FUTURE PROSPECTS

5.1 Summary

All the pulsed-current electrodeposited FM-NM and FM-FM granular alloys prepared using the computer-controlled pulsed-current electro-deposition method exhibited interesting spin-dependent MR, microstructure and particle size dependent MR and magnetization. Deposition current density in turn playing a great role in defining the shape of the precipitated particles and their size distribution.

The MR effect of pulsed-current deposited ferromagnetic-nonmagnetic granular alloys is found to be comparable to or larger than the MR effect observed in some vapor deposited alloys and by multilayered alloys. The Co-Ag alloys showed a large MR as compared to the MR displayed by Co-Cu, Co-Au, and Fe-Cu alloys. The MR of Co-Ag alloys increased with deposition current density used during the course of preparing these alloys. However, on annealing, it decreased significantly. Also, it seems that in the as-deposited state the Co-Ag alloys are already in the stage of phase-separation, and when annealed no effect on particle size and shape was observed.

The MR ratio of the Co-Cu alloys did not change with the deposition current density. However, it increased after annealing. It suggested that the as-deposited Co-Cu alloy films have been in a solid solution state, and that the deposition current seem to play no significant role in crystallographic orientation, film formation, film texture and quality. Likewise, the Co-Au alloys prepared at higher current density exhibited a large MR. However, the MR of Fe-Cu alloys is always found to be minimal as compared to the MR of Co-Cu or Co-Ag or Co-Au alloys. Interestingly, Fe-Cu alloys exhibited transformation from the bcc to fcc phase at 80 at. % Fe. In all cases, the MR and the grain sizes are found to be largely dependent on deposition current density.

The microstructure analysis suggested the presence of strong fcc-Cu, fcc-Ag and fcc-Au structures in these alloyed films imbedded with precipitates of fine grains that exhibit super-paramagnetic behavior. The temperature dependence of zero-field-cooled and field-cooled magnetizations for both the as-deposited and annealed alloys revealed the presence of smaller sized Co grains / particles in these alloy films, and in particular when they were deposited at higher current density. Based on these measurements, it can be confirmed that the increase in MR of the pulsed-current deposited alloys was due to the formation of alloys of better magnetic
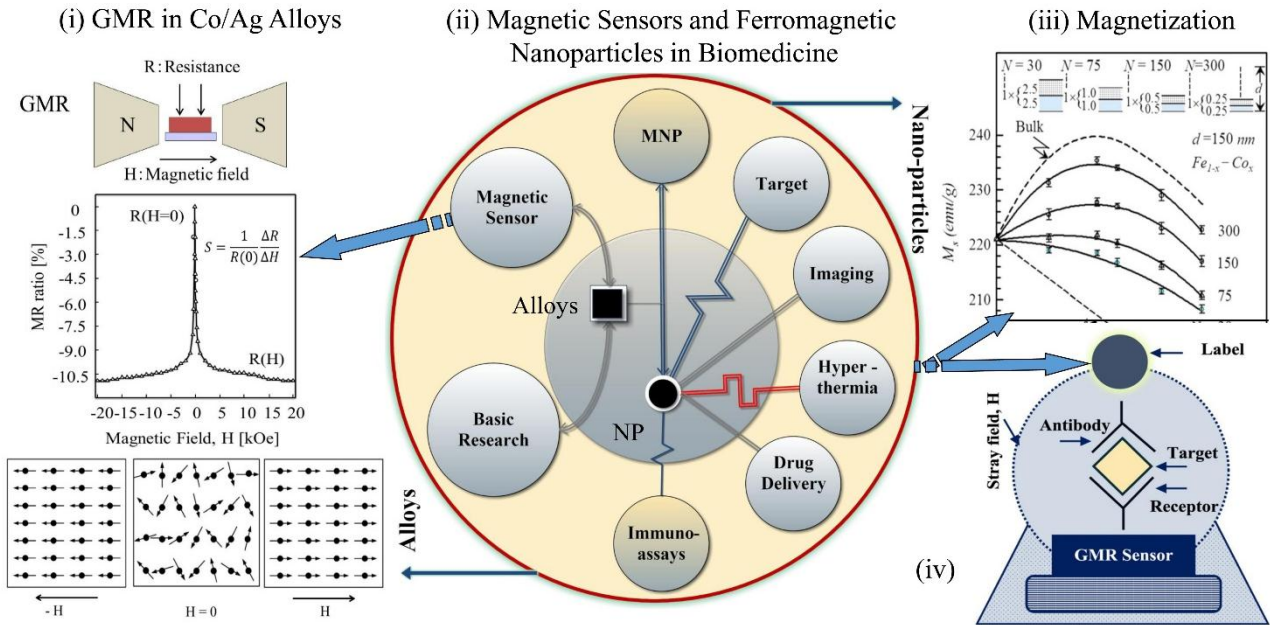
Fig. 12 – (i) Magnetic sensor [116], (ii) Functionalities of magnetic nanostructures/nanoparticles (MNPs), (iii) Magnetization of Fe-Co [8] and (iv) MNPs for diagnostics [117]

properties and smaller grain sizes. The saturation magnetization of all the alloys is found to be strongly dependent on the atomic composition and crystalline lattice constant, and these results are in line with the *Vegard's law* for the FM-NM alloys and empirical laws for the FM-FM alloys [115].

5.2 Potential Applications

The ferromagnetic-nonmagnetic alloys have been already found significant technological applications, as AMR sensors, especially as a speed sensor in automotive industry. Likewise, the GMR sensing principle has been already used for making read head sensor in computers. Applications of these alloys have significantly improved the storage density of hard disk drives. The applications of GMR sensing can be extended to making devices such as high speed high density memory. In fact, the use of GMR sensors is already growing in automotive applications such as, robotics, automation control, and detection of incremental increase of speed and position due to their high sensitivity and small sizes and more are forth coming.

The Fe-Co alloys reviewed here produced using computer controlled pulsed-current deposition technique, showed the highest saturation magnetization at room temperature compared to all other ferromagnetic-ferromagnetic alloys. The giant saturation magnetization was found to be directly related to number of film layers and stacking (bilayer) number, alloy composition and to the crystal lattice size. Due to the quantum well states of the nano-structured Fe-Co alloys produced using pulsed current deposition, these alloys are expected to exhibit unique physical properties that cannot otherwise be observed in bulk ferromagnetic-nonmagnetic and ferromagnetic-ferromagnetic alloys. In fact, the large saturation magnetization of 240 emu/gm observed for FM-FM alloys presented in this review, can in principle provide foundation for de-

veloping a commercially viable procedure for producing similar material in much larger scale. These nanoparticles have great potential to be used as bimolecular labels as nanotags, especially due to their comparable sizes to and compatibility with biomolecules.

Ferromagnetic alloys can also be potentially employed in making biomagnetic devices using ultra-fast and highly sensitive MR sensors and high saturation magnetization nano- and micro-sized alloys and particles and these can be fabricated using the method employed in this review, which is shown in Fig. 12 (i-iii). These nano- and micro- sized alloy structures with high MR and high saturation magnetization, can also be used in biology and medicine as they are biocompatible. Conventional bio-sensing technologies suffers from poor sensitivity.

Fig. 12(ii) shows various possible functionalities that can be achieved by combining the magnetic sensor and high saturation magnetization nanostructures. On other area where the FM sensors and magnetic nanoparticles (MNPs) have found active application is in early disease detection. This is shown in Fig. 12 (iv) where the magnetic sensor is equipped with a capture antibody (receptor) that is highly specific to a particular protein bio-marker (antibody) and then functionalized with the MNPs. In real time, the captured antibody conjugated with the MNPs (the stray H field is shown by dotted line) is quantitatively detected by underlying magnetic sensor.

Another area in which ferromagnetic nanostructures may find application is in medical imaging where the MNPs are first modified for bio-compatibility and then guided to the targeted locations as contrast agents for either already available MRI or for future MNPs-based imaging. In addition, using alternating magnetic fields, MNPs can be used for therapeutics, such as hyperthermia. Likewise, biocompatible MNPs when functionalized with biomarkers, can be used as drugs that can be released in response to the magnetic, optical,

thermal, and pH stimuli. The same can be useful for ultra-immunoassay where small samples, e.g., blood, can be used to concentrate the signal.

Except for the biochip-based detection system (similar to shown in Fig. 12(iv), all other biomagnetic techniques for medical applications are still at the proof-of-concept stage. Nevertheless, with the continuous improvement in nano-fabrication, characterization, and imaging techniques, we should see great advances in biomedical nano-magnetics such as metal alloys in the coming years. To realize full potential of magnetic alloys in new technologies, various physical and chemical principles of the ferromagnetic materials and their impacts on bio-medical imaging, bio-physics, energy, drug delivery, hypothermia, and immuno-assays, and a wide variety of other medical applications must be explored.

5.3 Future Prospects

Sensors based on FM-NM alloys are continuously gaining interest for industrial applications as they offer some intrinsic advantages such as small sizes and GMR effects at relatively small magnetic fields compared to AMR sensors and Hall effect based sensors. The room temperature sensitivity of GMR based sensors is also much larger than the sensitivity of Hall effect or AMR sensors. With the constant improvement in state-of-the-art processing and closely controlled manufacturing capabilities, the sensitivity of these alloys is expected to rise further.

The FM-FM alloys described in this review have exhibited superparamagnetic-like behaviors and the films deposited at higher current densities are found to contain smaller Co grain precipitates in resulting alloy films. These grains are highly conducive to molecular binding processes, free of magnetic agglomeration. These kinds of behaviors make them suitable for applications in many technological fields. The areas where

these super-paramagnetic like grains can have potential use are biomagnetic sensing, hyperthermia, magnetic imaging, drug-delivery, etc. All results presented in this review can be used as basis for developing magnetronic and biomagnetic technologies that can be used in improving early detection and treatment of various chronic diseases, including cancer. However, to develop potentially useful future technology and devices, strong collaboration between electrical engineers, physicists, and biologists and / or chemists is necessary.

The pulsed-current deposition method described in this review further opens up the potential future application of Ferromagnetic alloys in new industries. Since, conventional bio-sensing technologies suffers from poor sensitivity, nano and micro-sized alloy structures with higher magnetization can also be used in biology and medicine as they are bio compatible. In addition, the technique described in this review can be extended to produce new bio-functional magnetic nanowires or nanorods, quantum dots, etc., in complex geometries that are not usually possible via constant current electrodeposition, rf-sputtering, molecular beam epitaxy, or e-beam evaporation methods. Similarly, the technique used to produce high magnetic moment alloys described in this review can be extended to other granular alloys, nanoparticles, and multilayer systems that have not been covered in this review but deserve full consideration in the future.

REFERENCES

1. A. Fert, L. Piraux, *J. Magn. Magn. Mater.* **200**, 338 (1999).
2. A.E. Berkowitz, J.R. Mitchell, M.J. Carey, A.P. Young, S. Zhang, F.E. Spada, F.T. Parker, A. Hutten, G. Thomas, *Phys. Rev. Lett.* **68**, 3745 (1992).
3. J.Q. Xiao, J.S. Jiang, C.L. Chien, *Phys. Rev. Lett.* **68**, 3749 (1992).
4. S. Ikeda, T. Houga, W. Takakura, Y. Ueda, *Mater. Sci. Eng. A* **217**, 376 (1996).
5. J. Wang, G. Xiao, *Phys. Rev. B* **49**, 3982 (1994).
6. Y. Ueda, S. Ikeda, Y. Mori, H. Zaman, *J. Mater. Sci. Eng. A* **217**, 371 (1996).
7. H. Zaman, A. Yamada, H. Fukuda, Y. Ueda, *J. Electrochem. Soc.* **145**, 565 (1998).
8. C. Rizal, J. Kolthammer, R.K. Pokharel, B.C. Choi, *J. Appl. Phys.* **113**, 113905 (2013).
9. C. Rizal, *Magnetic and Microstructure of the Co-Au Nanostructures* 2nd International Conference on Nanotechnology: Fundamentals and Applications, Ottawa, Ontario, Canada. pp. 1-7. (July 27-29, 2011).
10. C. Rizal, S. Ishida, A. Yamada, Y. Ueda, *Jpn. J. Surf. Fin. Soc.* **55**, 83 (2004).
11. N. Thangaraj, C. Echer, K.M. Krishnan, R. Farrow, R. Marks, S. Parkin, *J. Appl. Phys.* **75**, 6900 (1994).
12. T. McGuire, R. Potter, *IEEE Trans. Magn.* **11** No 4, 1018 (1975).
13. T.G.M. Rijks, R. Coehoorn, M.J.M. De-Jong, W.J.M. De Jonge, *Phys. Rev. B* **51**, 283 (1995).
14. S. Kokado, M. Tsunoda, K. Harigaya, A. Sakuma, *The Phys. Soc. Jpn.* **81**, 024705 (2012).
15. Z. Celinski, B. Heinrich, *Phys. Rev. Lett.* **65**, 1156 (1990).
16. S.X. Wang, G. Li, *IEEE T. Magn.* **44** No 7, 1687 (2008).
17. J.M.D. Coey, *Magnetism and Magnetic Materials, 1st ed.* (Cambridge University Press: Cambridge: 2010).
18. B. Heinrich, J.A.C. Bland, *Ultrathin Magnetic Structures II* (Springer Science: 1994).
19. Y. Jing, S. He, T. Kline, Y. Xu, J.P. Wang, *High-Magnetic-Moment Nanoparticles for Biomedicine* (2009).
20. K.M. Krishnan, *IEEE T. Magn.* **46** No 7, 2523 (2010).
21. G. Reiss, H. Brueckl, A. Huetten, J. Schotter, M. Brzeska, M. Panhorst, D. Sudfeld, A. Becker, P.B. Kamp, A. Puehler, *J. Mater. Res.* **20**, 3294 (2005).
22. S. Ikeda, J. Hayakawa, Y.M. Lee, R. Sasaki, T. Meguro, F. Matsukura, H. Ohno, *Jpn. J. Appl. Phys.* **44**, L1442 (2005).
23. J. Smith, *J. Phys.* **17**, 6 (1951).
24. H.M. Jaeger, D.B. Haviland, B.G. Orr, A.M. Goldman, *Phys. Rev. B* **40**, 182 (1989).
25. S. Kokado, M. Tsunoda, K. Harigaya, A. Sakuma, *J. Phys. Soc. Jpn.* **81**, 024705 (2012).
26. I. Campbell, A. Fert, O. Jaoul, *J. Phys. C: Solid State Phys.* **3**, S95 (1970).
27. A. Malozemoff, *Phys. Rev. B* **32**, 6080 (1985).
28. M. Tsunoda, H. Takahashi, S. Kokado, Y. Komasaki, A. Sakuma, M. Takahashi, *Appl. Phys. Exp.* **3** No 11 113003 (2010).

29. M.N. Baibich, J.M. Broto, A. Fert, F.N. Van Dau, F. Petroff, P. Etienne, G. Creuzet, A. Friederich, J. Chazelas, *Phys. Rev. Lett.* **61**, 2472 (1988).

30. G. Binasch, P. Grünberg, F. Saurenbach, W. Zinn, *Phys. Rev. B* **39**, 4828 (1989).

31. E.E. Fullerton, M. Conover, J. Mattson, C. Sowers, S. Bader, *Appl. Phys. Lett.* **63**, 1699 (1993).

32. A.E. Berkowitz, J.R. Mitchell, M.J. Carey, A.P. Young, D. Rao, A. Starr, S. Zhang, F.E. Spada, F.T. Parker, A. Hutten, G. Thomas, *J. Appl. Phys.* **73**, 5320 (1993).

33. E. Ferrari, F. Da Silva, M. Knobel, *Phys. Rev. B* **59**, 8412 (1999).

34. S.S.P. Parkin, *Mater. Lett.* **20**, 1 (1994).

35. K. Takanashi, J. Park, T. Sugawara, K. Hono, A. Goto, H. Yasuoka, H. Fujimori, *Thin Solid Films* **275**, 106 (1996).

36. Y. Ueda, M. Ito, *Jpn. J. Appl. Phys.* **33**, L1403 (1994).

37. Y. Ueda, N. Hataya, H. Zaman, *J. Magn. Magn. Mater.* **156**, 350 (1996).

38. Y. Ueda, T. Houga, H. Zaman, A. Yamada, *J. Solid. State Chem.* **147**, 274 (1999).

39. A. Yamada, M. Shirota, T. Houga, C. Rizal, Y. Ueda, *Jpn. Inst. Metal.* **66**, 869 (2002).

40. A. Yamada, C. Rizal, S. Murata, Y. Ueda, *Jpn. J. Appl. Surf. Fin.* **55**, 151 (2004).

41. C. Rizal, Y. Ueda, B.R. Karki, *J. Nano- Electron. Phys.* **4** No 1, 01001 (2012).

42. I. Bakonyi, *Prog. Mater. Sci.* **55**, 107 (2010).

43. N. Kurti, *Selected Works of Louis Neel* (CRC Press: 1988).

44. W. Coffey, P. Cregg, Y. Kalmykov, *Adv. Chem. Phys.* **87**, 263 (1993).

45. C. Rizal, Y. Ueda, R.K. Pokharel, *Int. J. Appl. Phys. Math.* **1** No 3, 161 (2011).

46. C. Chien, *Annu. Rev. Mater. Sci.* **25**, 129 (1995).

47. H. Okamoto, T. Massalski, T. Nishizawa, M. Hasebe, *J. Phase Equilibria* **6** No 5 449 (1985).

48. O. Karaagac, H. Kockar, M. Alper, *IEEE Trans. Magn.* **46** No 12, 3973 (2010).

49. S. Kenane, J. Voiron, N. Benbrahim, E. Chainet, F. Robaut, *J. Magn. Magn. Mater.* **297**, 2 (2006).

50. J. Barnard, S. Hossain, M. Parker, A. Waknis, M. Watson, *J. Appl. Phys.* **73**, 6372 (1993).

51. J. Childress, C. Chien, *J. Appl. Phys.* **70**, 5885 (1991).

52. J. Garcia-Torres, E. Gómez, E. Vallés, *Mater. Chem. Phys.* **122**, 463 (2010).

53. N.A. Spaldin, *Magnetic Materials: Fundamentals and Applications* (Cambridge University Press: 2010).

54. J.P. Liu, E. Fullerton, O. Gutfleisch, D.J. Sellmyer, *Nanoscale Magnetic Materials and Applications* (Springer: 2009).

55. C. Jo, J.I. Lee, Y. Jang, *Chem. Mater.* **17**, 2667 (2005).

56. L. Sun, Y. Hao, C. Chien, P.C. Searson, *IBM J. Res. Develop.* **49** No 1, 79 (2005).

57. J. Pierce, E. Plummer, J. Shen, *Appl. Phys. Lett.* **81**, 1890 (2002).

58. T.L. Kline, Y.H. Xu, Y. Jing, J.P. Wang, *J. Magn. Magn. Mater.* **321**, 1525 (2009).

59. A.D. Romig, J. Goldstein, *Metallurgical Transactions A* **11** No 7, 1151 (1980).

60. T. Nishizawa, K. Ishida, *Bull. Alloy Phase Diagrams* **5**, 3 (1984).

61. H. Okamoto, *Phase Diagrams of Dilute Binary Alloys* (ASM International Materials Park: OH: 2002).

62. I. Ohnuma, H. Enoki, O. Ikeda, R. Kainuma, H. Ohtani, B. Sundman, K. Ishida, *Acta Materialia* **50**, 379 (2002).

63. M. Baricco, E. Bosco, G. Acconciaioco, P. Rizzi, M. Coisson, *Mater. Sci. Eng. A* **375-377**, 1019 (2004).

64. F. Badia, X. Batlle, A. Labarta, M. Watson, A. Johnston, J. Chapman, *J. Appl. Phys.* **82**, 677 (1997).

65. H.C. Chang, Y.H. Chang, S.Y. Yao, *J. Appl. Phys.* **82**, 317 (1997).

66. V. Franco, X. Batlle, A. Valencia, A. Labarta, K. O'Grady, M.L. Watson, *IEEE Trans. Magn.* **34**, 912 (1998).

67. M. Kitada, *J. Magn. Magn. Mater.* **208**, 244 (2000).

68. S.R. Teixeira, B. Dieny, A. Chamberod, C. Cowache, S. Auffret, P. Auric, J.L. Rouviere, O. Redon, J. Pierre, *J. Phys.: Condens. Matt.* **6**, 5545 (1994).

69. H. Sato, Y. Kobayashi, Y. Aoki, H. Yamamoto, *J. Phys.: Condens. Matt.* **7**, 7053 (1995).

70. E.I. Cooper, C. Bonhote, J. Heidmann, Y. Hsu, P. Kern, J.W. Lam, M. Ramasubramanian, N.M. Robertson, L.T. Romankiw, H. Xu, *IBM J. Res. Dev.* **49**, 103 (2005).

71. A. Robertson, U. Erb, G. Palumbo, *Nanostruct. Mater.* **12**, 1035 (1999).

72. C.A. Ross, *Annu. Rev. Mater. Sci.* **24**, 159 (1994).

73. A. Brenner, *Electrodeposition of Alloys Principle and Practice* (Academic Press: 1963).

74. M. Guan, E.J. Podlaha, *J. Appl. Electrochem.* **37** No 5, 549 (2007).

75. Z. Guo, M. Moldovan, D. Young, L. Henry, E.J. Podlahad, *Electrochem. Solid-State Lett.* **10** No 12, E31 (2007).

76. E. Santos Jr, M. Abbate, V. Fernandes, N. Mattoso, *Electrochem. Solid-State Lett.* **6**, C85 (2003).

77. Z.J. Huba, K.J. Carroll, E.E. Carpenter, *J. Appl. Phys.* **109**, 07B514 (2011).

78. L. Peter, A. Cziraki, L. Pogany, Z. Kupay, I. Bakonyi, M. Uhlemann, M. Herrich, B. Arnold, T. Bauer, K. Wetzig, *J. Electrochem. Soc.* **148**, C168 (2001).

79. N. Rajasekaran, S. Mohan, R. Jagannathan, *J. Magn. Magn. Mater.* **324**, 2983 (2012).

80. A. Yamada, T. Houga, Y. Ueda, *J. Magn. Magn. Mater.* **239**, 272 (2002).

81. C. Larson, J. Smith, *Trans. Institute Mater. Finish.* **89**, 6 (2011).

82. J.R. Roos, J. Celis, M. Bonte, *Mater. Sci. Technol.* (1991).

83. H. Natter, R. Hempelmann, *Electrochim. Acta* **49**, 51 (2003).

84. E. Tóth-Kádár, L. Péter, T. Becsei, J. Tóth, L. Pogány, T. Tarnóczi, P. Kamasa, G. Láng, Á. Cziráki, W. Schwarzacher, *J. Electrochem. Soc.* **147**, 3311 (2000).

85. I. Baskaran, T.S. Narayanan, A. Stephen, *Mater. Lett.* **60**, 1990 (2006).

86. C. Rizal, *Giant Magnetoresistance and Magnetic Properties of Ferromagnetic Hybrid Nanostructures, PhD ed.* (University of British Columbia: Vancouver: 2012).

87. C. Rizal, A. Yamada, Y. Hori, S. Ishida, M. Matsuda, Y. Ueda, *phys. status solidi c* **1**, 1756 (2004).

88. M. Chandrasekar, M. Pushpavanam, *Electrochim. Acta* **53**, 3313 (2008).

89. J. Puippe, F. Leaman, *Theory and Practice of Pulse Plating* (American Electroplaters Society, Inc.: 1986).

90. H. Zaman, S. Ikeda, Y. Ueda, *Magnetoresistance in Co-Ag Multilayers and Granular Films Produced by Electrodeposition Method, Korea ed.* (IEEE Magnetics: 1997).

91. C. Rizal, B. Moa, J. Wingert, O.G. Shpyrko, *IEEE Trans. Magn.* **51** No 2, 2001106 (2015).

92. S. Foner, *J. Appl. Phys.* **79**, 4740 (1996).

93. B.D. Cullity, S. Stock, *Elements of X-Ray Diffraction* (Prentice Hall: 1972).

94. E.E. Fullerton, I.K. Schuller, H. Vanderstraeten, Y. Bruynseraede, *Phys. Rev. B* **45**, 9292 (1992).

95. H. Karami, H. Babaei, *Int. J. Electrochem. Sci.* **7** No 1, 601 (2012).

96. I. Karakaya, W. Thompson, *J. Phase Equilibria* **7** No 3, 259 (1986).

97. T. Nishizawa, K. Ishida, *J. Phase Equilibria* **5** No 2, 161 (1984).

98. M. Björck, G. Andersson, *J. Appl. Crystallography* **40**, 1174 (2007).

99. C. Rizal, E.E. Fullerton, *IOP Journal* (in Preparation) (2016).

100. P. Allia, M. Baricco, M. Knobel, P. Tiberto, F. Vinai, *J. Magn. Magn. Mater.* **140-144**, 617 (1995).

101. N. Kataoka, H. Takeda, J. Echigoya, K. Fukamichi, E. Aoyagi, Y. Shimada, H. Okuda, K. Osamura, M. Furusaka, T. Goto, *J. Magn. Magn. Mater.* **140-144**, 621 (1995).

102. J. Zhang, M. Post, T. Veres, Z.J. Jakubek, J. Guan, D. Wang, F. Normandin, Y. Deslandes, B. Simard, *The J. Phys. Chem. B* **110**, 7122 (2006).

103. K. Attenborough, R. Hart, S. Lane, M. Alper, W. Schwarzacher, *J. Magn. Magn. Mater.* **148**, 335 (1995).

104. Z. Liang Bao, K.L. Kavanagh, *J. Cryst. Growth* **287**, 514 (2006).

105. J.P. Wang, *Proc. IEEE* **96**, 1847 (2008).

106. A. Karpuz, H. Kockar, M. Alper, O. Karaagac, M. Haciismailoglu, *Appl. Surf. Sci.* **258**, 4005 (2012).

107. M. Niinomi, *Metallurgical Mater. Trans. A* **33** No 3, 477 (2002).

108. R. Victora, L. Falicov, *Phys. Rev. B* **30**, 1695 (1984).

109. R. Victora, L. Falicov, *Phys. Rev. B* **31**, 7335 (1985).

110. T. Sourmail, *Prog. Mater. Sci.* **50**, 816 (2005).

111. M. Takahashi, H. Shoji, *J. Magn. Magn. Mater.* **208**, 145 (2000).

112. J. Coey, *J. Appl. Phys.* **76**, 6632 (1994).

113. N. Ji, X. Liu, J. Wang, *New J. Phys.* **12**, 063032 (2010).

114. L. Ke, K.D. Belashchenko, M. van Schilfgaarde, T. Kotani, V.P. Antropov, *Phys. Rev. B* **88**, 024404 (2013).

115. M. Shiga, *J. Phys. Soc. Jpn.* **50**, 2573 (1981).

116. C. Rizal, Y. Ueda, *IEEE T. Magn.* **45** No 6, 2399 (2009).

117. D. Hall, R.S. Gaster, K. Makinwa, S.X. Wang, B. Murmann, *IEEE J. Solid-State Circuits* **48** No 5, 1290 (2013).